Geomech. Geophys. Geo-energ. Geo-resour. (2024) 10:38
https://doi.org/10.1007/s40948-024-00749-x

ORIGINAL ARTICLE

Rockburst prevention by microwave destressing: a numerical investigation

Chun Yang · Keping Zhou · Quan Zhang · Manchao He · Feng Gao · Xin Xiong · Zheng Pan · Ameen Topa

Received: 22 July 2022 / Accepted: 10 January 2024

Abstract Rockbursts are a complex phenomenon characterized by a violent ejection of rock fragments from the free face of deep underground mines. Due to the sudden, disruptive, and complex nature of these events, accurate predictions of rockbursts are difficult. Therefore, geotechnical intervention is imperative to prevent the occurrence of a rockburst. The scenarios of microwave destressing is introduced here as an application method to potentially prevent their occurrence. To understand the influences of microwave destressing, such as microwave exposure duration, spatial layout, and geometric parameters of the microwave preconditioned zone (MPZ), on the occurrence of a rockburst, numerical simulation was conducted based on an impact-induced rockburst model. The feasibility of microwave destressing technology was validated numerically. This paper also provides guidance for the utilization of microwave destressing in practice. Discontinuous MPZ is suitable for a known blasting source with a fixed position, and continuous MPZ can be applied for a working condition with multiple blasting sources with variable positions. A closer distance of MPZ from the free face results in a better microwave destressing effect. However, the closer distance of MPZ from the free face also introduces more negative influences on the static stability of surrounding rock.

Highlights

- Microwave destressing scenario is introduced.
- The feasibility of microwave destressing in deep circular openings is numerically validated.
- The principle of rockburst prevention via microwave preconditioning is summarized.

C. Yang · K. Zhou · F. Gao · X. Xiong · Z. Pan
School of Resources and Safety Engineering, Central South University, Changsha 410083, Hunan, China

C. Yang
Department of Mining and Materials Engineering, McGill University, Montreal H3A2A7, Canada

Q. Zhang (✉)
School of Mines, China University of Mining and Technology, Xuzhou 221116, Jiangsu, China
e-mail: zhangquan@cumt.edu.cn

Q. Zhang
State key Laboratory of Mining Disaster Prevention and Control (Shandong University of Science and Technology), Ministry of Education, Qingdao, 266590, Shandong, China

M. He
School of Mechanics and Civil Engineering, China University of Mining and Technology, Beijing 100083, China

A. Topa
Department of Maritime Technology, Faculty of Ocean Engineering Technology and Informatics, Universiti Malaysia Terengganu, 21030 Kuala Terengganu, Malaysia

Published online: 03 February 2024

- The spatial layout and geometrical parameters of MPZ significantly affect the microwave destressing effect.

Keywords Rockburst prevention · Microwave destressing · Strain energy density (SED) · Dynamic failure · Dynamic disturbance

1 Introduction

In deep rock engineering excavation, the violent failure of a rock mass, termed rockburst, significantly threatens personnel and machine safety. Thus, containing rockbursts has become the most challenging task for engineers (Khan et al. 2021; Pan et al. 2022; Sainoki et al. 2017; Wang et al. 2022). Many scholars have conducted in-situ and laboratory tests to investigate rockburst phenomena, which revealed that factors including underground geometry and geology play vital roles in the occurrence of rockbursts (Guo et al. 2021; He et al. 2018; Manouchehrian and Cai 2018; Mazaira and Konicek 2015). According to the triggering mechanisms, rockbursts can be classified into two major types: strainbursts and impact-induced rockbursts (He et al. 2012). Strainbursts at the edge of openings are caused by high in-situ stress regimes that exceed the rock strength (Cai 2019; Vazaios et al. 2019). Impact-induced rockbursts mainly generate when the surrounding rocks in a relatively low-stress state are impacted by external dynamic disturbances, such as blasting, caving, and mechanical vibration (Li and Li 2018; Li et al. 2020a). Therefore, both the high stress zone shifting far from the free face and constructing a protective barrier between the working face and the dynamic disturbance could effectively contain rockbursts.

Geotechnical measures such as destress blasting, destress drilling, shotcrete and mesh (Mazaira and Konicek 2015), pre-excavation grouting (Zhang et al. 2014), seismic monitoring (Tang et al. 2023b), TBM excavation (Gong et al. 2012), and water infusion have been widely used to deal with the damaging effects of rockbursts (Konicek et al. 2011; Xu et al. 2022). Among these methods, a proactive measure termed destress blasting has been applied for nearly a century. A fractured zone is formed by blasting behind the tunnel face. Consequently, the stiffness reduction of the rock mass in the fractured zone induces the second stress redistribution. Face destressing is achieved under the influence of the maximum stress behind the tunnel face decreasing and its position shifting away from the initial position (Vennes et al. 2021). However, it is worth noting that destress blasting introduces a dynamic disturbance to the high in-situ stress zone around the tunnel. An unreasonable destress blasting scheme can even cause the opposite desired effect. The essence of destress blasting is to reduce the rock strength and create a network of fissures in the target area by blasting (Drover et al. 2018). Therefore, the utilization of other rock breakage technology may also induce a destressed zone. Furthermore, the lower the stress disturbance induced by rock breakage, the more suitable it is for destressing.

Over the past two decades, microwave-assisted rock breakage has attracted much attention, which is regarded as a promising technology in extending the service life of cutter and space mining (Li et al. 2020b; Wang et al. 2021; Yang et al. 2022b, 2022c). Microwave heating mechanism to weaken rock has been shown in both experimental and numerical tests (Jones et al. 2005; Ju et al. 2021; Lu et al. 2019b). The majority of rocks are typically a mixture of several different minerals, and each mineral shows different dielectric properties, volumetric expansion, and thermal conductivity (Zheng et al. 2020). Microwave heating can generate significant heat in rocks containing microwave-absorbing minerals such as biotite, hornblende, hypersthene, enstatite, etc. (Lu et al. 2017; Zhao et al. 2020). This process introduces a temperature gradient into the rock, leading to the generation of stress that may exceed the rock's strength. Therefore, micro-cracks are generated within the rocks, and if the rock is treated with a significant enough microwave power level or for a long enough exposure time, visible macro-cracks can form (Meisels et al. 2015). Furthermore, adjacent grains with differing dielectric properties enhance crack formation. Accordingly, the rock strength decreases after microwave treatment (Kahraman et al. 2020).

Scholars have been aware of the possibility of pressure-relief around a deep rock opening caused by microwave preconditioning technology (Feng et al. 2017; Tang et al. 2023a; Zhang et al. 2022). Referring to the destress blasting scenario, the microwave destressing concept, as Fig. 1 depicts, can be classified into face, roof, floor and side wall destressing.

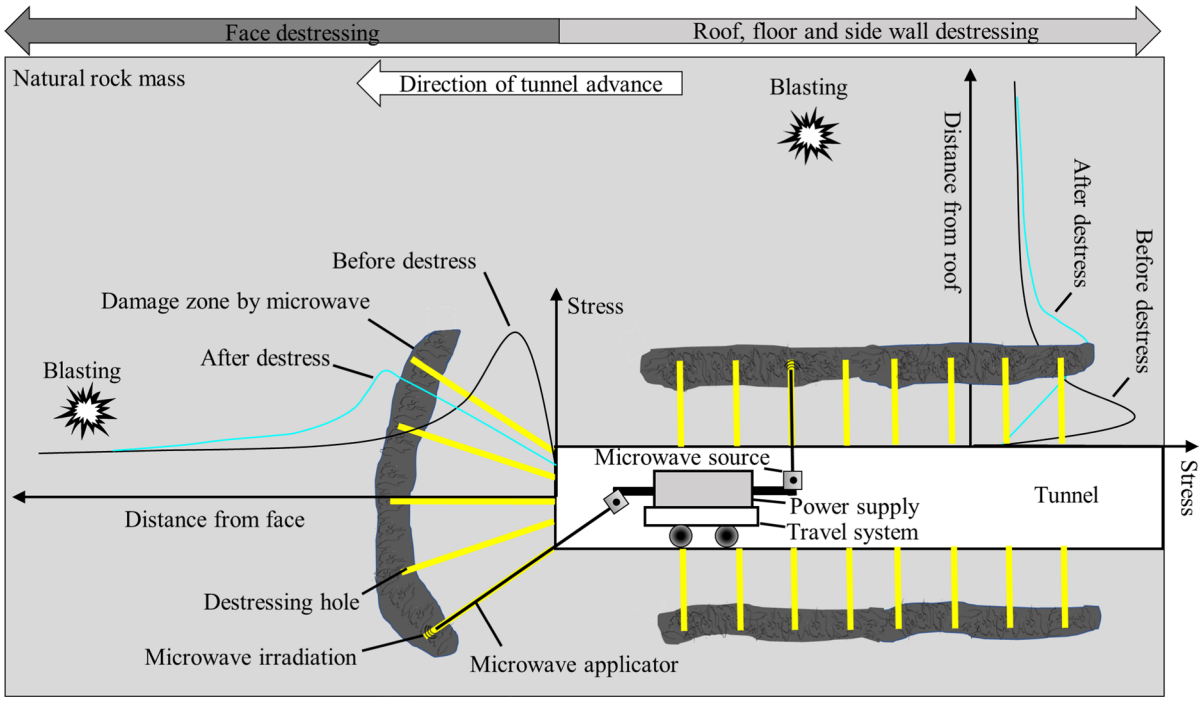

Fig. 1 Schematic diagram of rockburst containment in deep rock engineering using microwave destressing

Microwave energy is applied to the target zone via the borehole. Lu et al. (2019a) developed a coaxial-type microwave applicator for borehole fracturing, which effectively induces macro-cracks in cubic hard rock specimens in lab tests. Moreover, field tests with this apparatus exhibit a favorable fracturing effect (3–7 cm obvious fractures were observed by the digital borehole televiewer) on boreholes in the Baihetan Hydropower Station. Feng et al. (2021) conducted microwave irradiation tests on hard rocks under true triaxial stress with an open-ended microwave-induced fracturing system. This novel experimental setup can approximately simulate the utilization of microwaves in a high-stress environment. The experimental results of borehole fracturing tests indicate that true triaxial stress facilitates the distribution of thermal cracks induced by microwave treatment. Hu et al. (2021) carefully evaluated the burst tendency of microwave-treated hard coal using indicators such as the dynamic failure time, impact energy index, elastic index, uniaxial compressive strength (UCS), and P-wave velocity, which illustrated that microwave preconditioning could effectively reduce or eliminate the burst tendency of coal. Generally, the existing studies involved with rockburst prevention using microwave precondition technology mainly focus on the rockburst proneness of a microwave treated hard rock itself. The influence of the microwave preconditioned zone (MPZ) on stress distribution in its surrounding rock and how it can achieve rockburst prevention in an existing rock engineering are rarely reported.

The primary focus of this paper is to determine the effect of MPZ layout on rock failure subjected to a dynamic disturbance around a deep circular opening using numerical analysis. The rock strain energy density (SED) and dynamic failure intensity of the failure zone in different simulation cases are carefully evaluated based on an impact-induced rockburst model. It also aims to provide reasonable suggestions for the utilization of microwave destressing technology in practice.

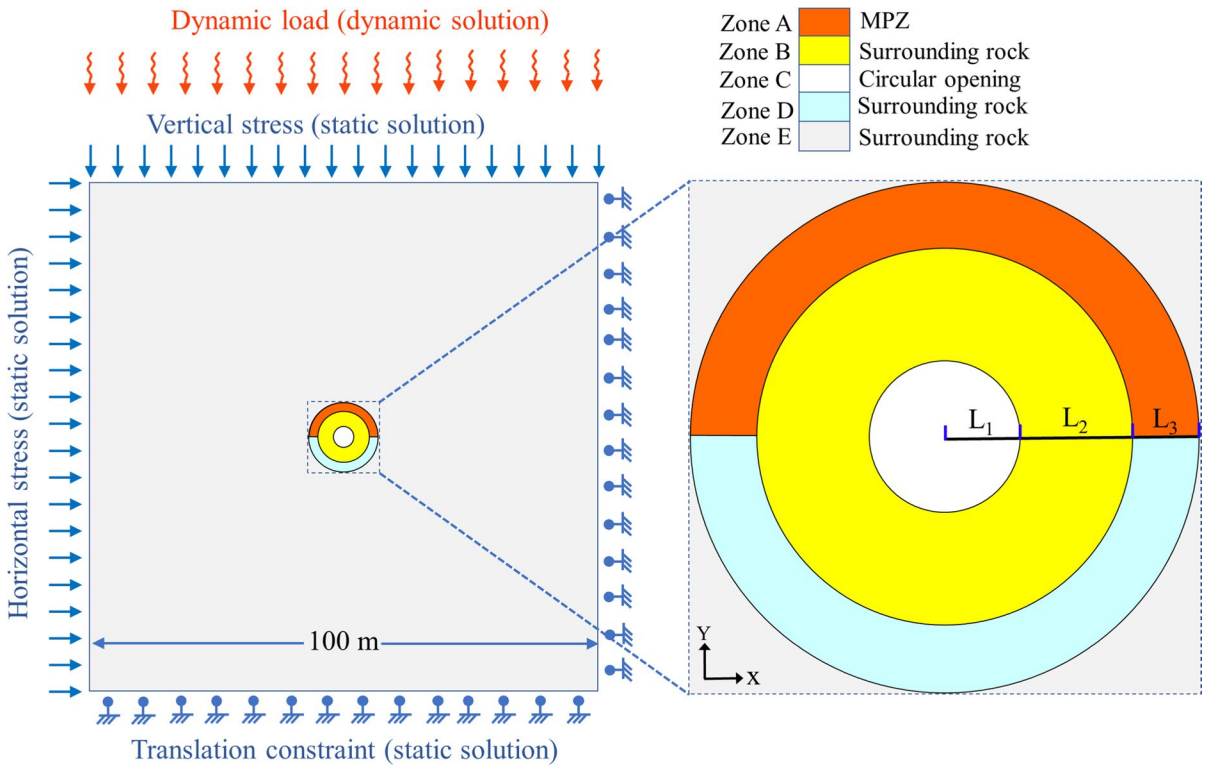

Fig. 2 Schematic of the numerical model setup showing the boundary conditions, model components and their physical representations

2 Numerical model parameters

2.1 Establishment of model

As Fig. 2 shows, a square, quasi-three-dimensional numerical model with a length of 100 m was created using the finite element method (FEM) (Yang et al. 2021). Roof destressing in a deep circular opening with a radius L_1 of 2 m was employed in the numerical simulation. Generally, rockbursts are influenced by gravity, and typically those that occur on the top can cause higher threats than those located towards the base of the opening. Thus, given the computing efficiency and the convenience of mesh generation, a semi-annular MPZ was arranged on the top of the opening, and another semi-circular section (zone D) with intact rock material was symmetrically distributed under zone A (Zhou and Xiao 2018, 2019). The radial distance between the sidewall of the opening and MPZ (L_2), and the radial length of MPZ (L_3) was varied for different simulation cases to determine their influences on rockbursts with microwave treatment.

2.2 Initial geo-stress and dynamic load

Impact-induced rockbursts are governed by the synergistic effect between geo-stress and the dynamic load. Studies have revealed that the geo-stress intensity and orientation, dynamic load duration and amplitude, and the duration ratio of dynamic loading and dynamic unloading significantly affect the rockburst characteristics (Li et al. 2018; Tang et al. 2019). The purpose of this study is to investigate the effects of different layouts of MPZ on rockburst prevention. Therefore, the vertical stress σ_v and horizontal stress σ_H were kept constant in all the simulation cases, which were determined by the following (Sheorey 1994),

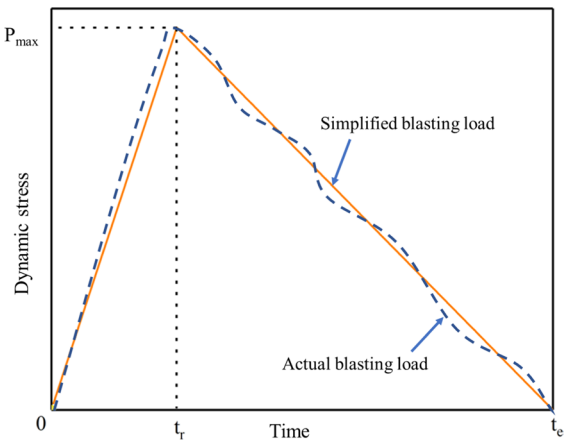

Fig. 3 Schematic diagram of the simplified blasting load applied to the top boundary during explicit solution

$$\sigma_v = \gamma H \tag{1}$$

$$\sigma_H = K\sigma_v \tag{2}$$

$$K = 0.25 + 7E_h\left(0.001 + \frac{1}{H}\right) \tag{3}$$

where H, K and E_h denote the depth (1000 m), initial stress ratio, and horizontal deformation modulus, respectively.

For an existing rock engineering project, blasting vibration is one of the primary sources of dynamic disturbance. The dynamic disturbance was applied at the top of the model by a simplified triangular load (Fig. 3), which can be expressed as the following (Hu et al. 2018):

$$P_d(t) = \begin{cases} 0, & t < 0 \\ \frac{t}{t_r} P_{\max}, & 0 \le t < t_r \\ \frac{t_e - t}{t_e - t_r} P_{\max}, & t_t \le t < t_e \\ 0, & t \ge t_e \end{cases} \tag{4}$$

where $P_{\max}$ is the peak value of the dynamic disturbance and t_e is the total duration of the triangular load. The rising stage duration varies from 0 to t_r and the peak value of the dynamic disturbance decreases from $P_{\max}$ at t_r to 0 at t_e. To trigger rockbursts under the previous geo-stress condition, $P_{\max}$, t_r and t_e were determined to 120 MPa, 2 ms, and 10 ms, respectively.

The finite element software LS-DYNA was employed to establish the numerical model. The simulation of impact-induced rockbursts employs a two-step process, namely implicit-explicit conversion. The initial step involves obtaining the initial geo-stress distribution within the rock using an implicit solution. Once the initial geo-stress is established, the simulation transitions to an explicit phase to introduce dynamic loading. In this transition, the displacement information obtained in the implicit phase is eliminated, retaining only the stress information. The triangular blasting load, as illustrated in Fig. 3, is applied to the top boundary of the model presented in Fig. 2 during the explicit solution.

2.3 Constitutive model and rock mechanical parameter verification

The Mohr–Coulomb model is most commonly applied in the context of geomaterials. It postulates a linear relationship between the shear strength on a plane and the normal stress acting on it. This can be represented by plotting Mohr's circles for stress states at the point of failure in terms of the maximum and minimum principal stresses (Fig. 4). The linear Mohr–Coulomb model can be written as:

$$\tau = c + \sigma \tan\phi \tag{5}$$

where τ is the shear stress, σ is the normal stress, c is the cohesion of the material, and ϕ is internal friction angle.

Lu et al. (2020, 2019b) conducted UCS and Brazilian tension strength (BTS) and conventional triaxial compressive strength (CTCS) tests of microwave-treated basalts at 5 kW microwave power level for

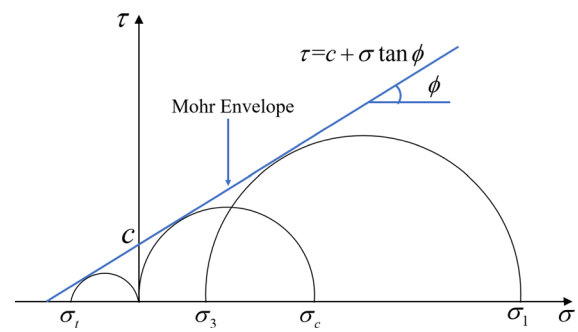

Fig. 4 Mohr–Coulomb Failure Envelope

Table 1 Basalt physical and mechanical parameters at 5 kW microwave power level

Case No	Exposure time (s)	Elastic modulus (GPa)	Poisson's ratio	Internal friction angle (°)	Cohesion (MPa)	UCS (MPa)	DTS (MPa)
A0	0	97.07	0.28	66.37	29.51	282.18	12.34
A1	10	86.54	0.26	67.21	25.78	255.90	10.39
A2	20	80.65	0.24	68.42	22.01	231.00	8.39
A3	30	74.76	0.22	70.02	18.15	206.10	6.39

various treatment times of 10 s, 20 s, and 30 s, respectively. Each exposure time trial was conducted three times for repetition. The linear regression analysis was summarized by relationships between the basalt strength, elastic modulus, Poisson's ratio, and microwave treatment times. The data from these analyses were used in this study.

As a natural material, rock contains natural flaws, such as joints, pores, and cracks. Although the effort has been made to reduce sampling error during experimental specimen preparation, microwave-induced damage (e.g., formation of irregular cracks in specimens) enhances differences within a sample, which would likely enhance the variations in the experimental results. However, in numerical modeling, it is assumed that rock is a homogeneous medium. For rock mechanical parameters, a compromise is to use the UCS, BTS, elastic modulus, Poisson's ratio obtained from lab tests, and the cohesion and internal friction angle is calibrated based on Mohr–Coulomb theory. As thus, the errors from the CTCS test can be eliminated.

In the triaxial stress state, the Mohr–Coulomb failure surface can be expressed as:

$$\frac{\sigma_1-\sigma_3}{2}=\frac{\sigma_1-\sigma_3}{2}\sin\ \phi+c\ \cos\ \phi \tag{6}$$

where σ_1 and σ_3 denote the major and minor principal stresses, respectively.

In a pure compression stress state, $\sigma_1=$UCS and $\sigma_3=0$, thus we have:

$$UCS=\frac{2c\ \cos\ \phi}{1-\sin\ \phi} \tag{7}$$

In a pure tension stress state, $\sigma_1=0$ and $-\sigma_3=$direct tension strength (DTS), thus we have:

$$DTS=\frac{2c\ \cos\ \phi}{1+\sin\ \phi} \tag{8}$$

Therefore, for a linear Mohr–Coulomb failure criterion, the UCS and DTS can be predicted by Eqs. (7) and (8) when the cohesion and internal friction angle are known. Because BTS represents the approximate tensile strength of rocks, DTS is calibrated by the following equation:

$$\mathrm{DTS}=f\ \mathrm{BTS} \tag{9}$$

where the value of the factor f is recommended to be approximately 0.8 for igneous rocks (Perras and Diederichs 2014).

Additional specific details regarding the calibration of mechanical parameters for microwave-treated basalt can be found in (Yang et al. 2022a). The calibrated mechanical parameters for basalt at a 5 kW microwave power level are listed in Table 1. To examine the accuracy of the calibrated mechanical parameters of a microwave treated basalt, UCS and DTS simulations were conducted to obtain the stress–strain relationships. Because of the advantages of high computing efficiency and the fact that it could eliminate unwanted structural effects, single element tests are widely used in mechanical parameter examination and verification of a developed constituted model. As shown in Fig. 5, a cubic element with eight nodes was employed to predict the compressive and tensile behaviors of microwave-treated basalt strengths using the Mohr–Coulomb material model. A constant motion was applied to the top four nodes following the intended loading pattern. Necessary constraints for specific nodes were considered to maintain the single element model's pure compression or tension stress state. In group A, four simulation cases (A0, A1, A2, and A3) were conducted with respect to different microwave exposure times, where cases A0, A1, A2, and A3 corresponding to the exposure time were 0, 10 s, 20 s, and 30 s, respectively.

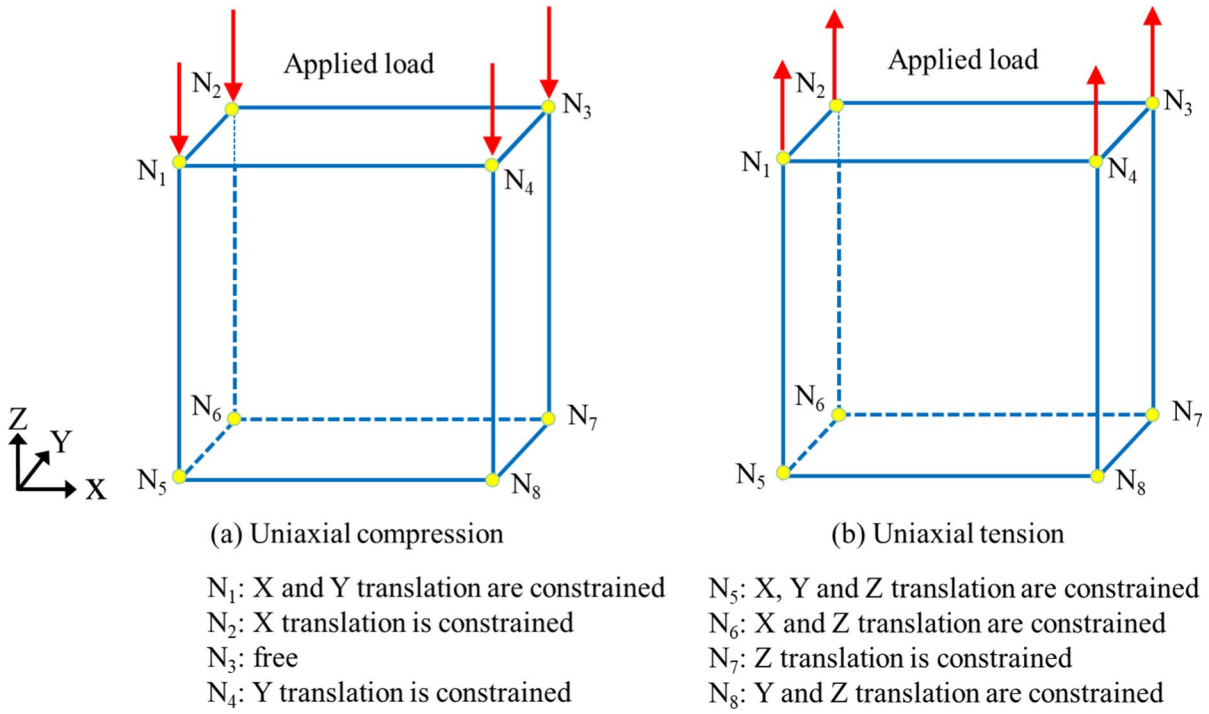

Fig. 5 Boundary conditions for the single element simulated model (modified after Guo et al. 2018)

The numerical results indicate that the UCS and DTS agree well with laboratory results (Fig. 6). Experimental UCS and BTS were simultaneously captured according to the same set of calibrated cohesion and internal friction angle data. In addition, the maximum axial strain in the UCS modeling was very similar to the experimental values (around 0.30%) (Lu et al. 2020). These results demonstrate the applicability of the calibrated mechanical parameters for the simulations involving microwave-treated basalt. More details of the numerical verification of microwave treated basalt strength with disc and cylinder sample can be found in (Yang et al. 2022a).

3 Analysis of microwave destressing

3.1 Geo-stress and strain energy redistribution

Referring to Saint–Venant's principle and the destress blasting application case (Luo et al. 2021), L_2 and L_3 were determined to be 3 m and 1 m in group A, respectively. As Fig. 7 shows, a monitoring line along the vertical central axis was used to track the stress distribution and energy variation caused by excavation and microwave preconditioning. Strain energy storage level in a rock mass significantly influences the induction of rockbursts (Zhang et al. 2021b). To eliminate the influence of size, strain energy density (SED) is often used to investigate the energy evolution surrounding the deep opening subjected to exterior dynamic impacting, which can be expressed as,

$$W = \frac{1}{2E}\left(\sigma_1^2 + \sigma_2^2 + \sigma_3^2 - 2\nu(\sigma_1\sigma_2 + \sigma_1\sigma_3 + \sigma_2\sigma_3)\right) \tag{10}$$

where W represents SED, E represents Young's modulus, and ν represents Poisson's ratio. σ_1, σ_2, and σ_3 are the maximum, intermediate, and minor principal stresses, respectively.

As Fig. 8a shows, the initial major and minimum principal stresses were − 21.17 MPa and − 46.60 MPa before excavation. In this section, the increase or decrease of principal stresses are in terms of their absolute values. After the excavation and microwave preconditioning, the redistributed stress around the opening was also in a compressive state. Compared with the stress state before excavation, the

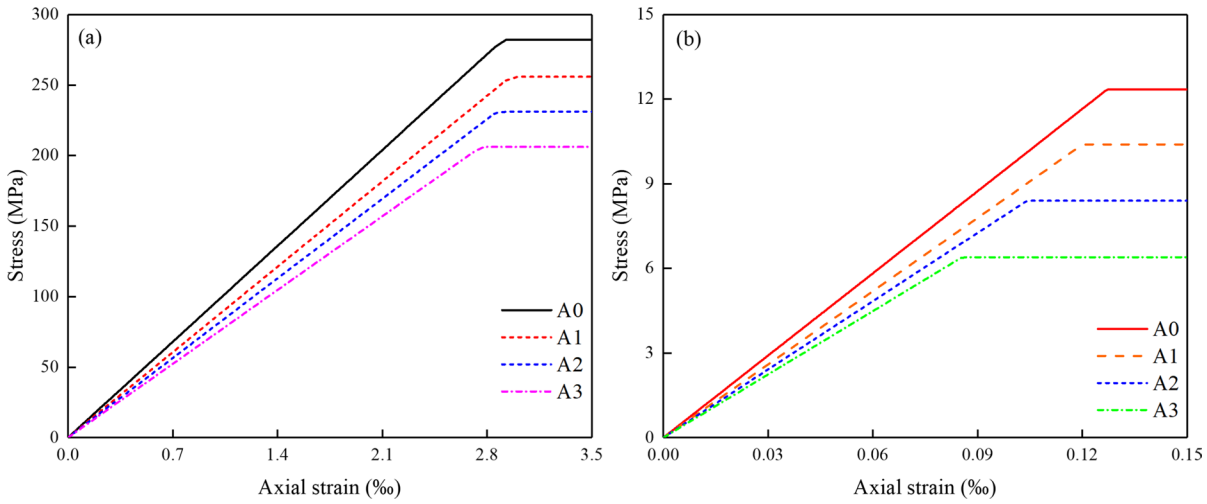

Fig. 6 Stress–strain curves of the UCS and DTS simulations using a single element test

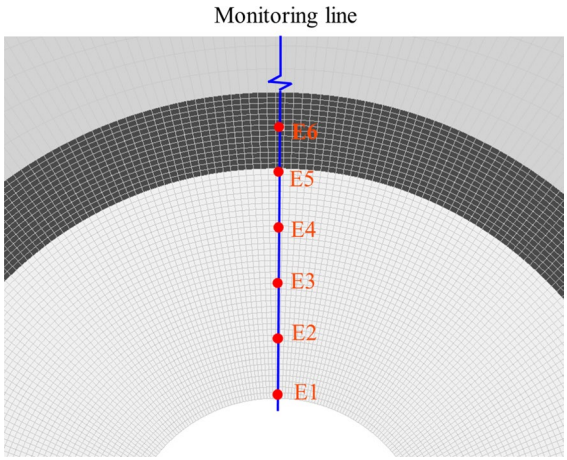

Fig. 7 Distribution of monitoring points and line for SED and stresses around the opening (cross sectional view)

stress redistribution significantly induced a decrease in the major principal stress (absolute value reduced to 19.63 MPa) and an increase in the minor principal stress (absolute value increased to 107.78 MPa) in the vicinity of the opening. The redistributed stress gradually approached an undisturbed stress state with an increase in the distance from the roof. Due to the different initial magnitude, the major principal stress reached a constant magnitude when the distance from the roof was approximately 10 m, and minor principal stress was approximately 16 m. Therefore, rock mass farther than 16 m from the roof was recognized as the undisturbed zone. According to the partially enlarged view in Fig. 8, the microwave preconditioning induced different stress redistributions at areas separated by the boundary of zone A and zone B. Compared to the A0 case, within 4 m to the roof, microwave treatment induced a decrease in the stress level. On the contrary, the microwave treatment induced an increase in the geo-stress level when the distance from the roof was greater than 4 m. In the MPZ, the stress magnitude declined with an increase in microwave exposure time. Overall, it appears that a longer microwave exposure time allows for a higher magnitude of stress redistribution.

As Fig. 8b shows, consistent with the rules governing the redistribution stress, the SED shows similar variation with a change in the distance from the roof. In MPZ and the surrounding rock zone B, microwave treatment induced a reduction in the SED. Overall, SED decreased with increasing distance from the roof. For specific rock properties, a lower SED has a lower rockburst risk when subjected to dynamic disturbance. Thus, it can be deduced by the static mechanical response of the rock mass that microwave destressing for rockburst prevention is feasible.

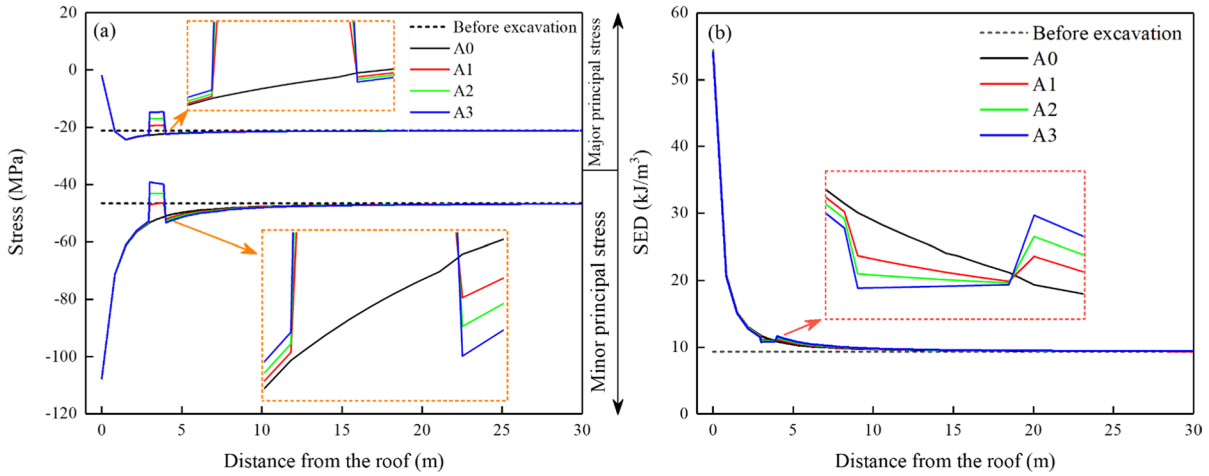

Fig. 8 Redistributions of principle stresses and SED in implicit solution. **a** Principal stresses; **b** SED

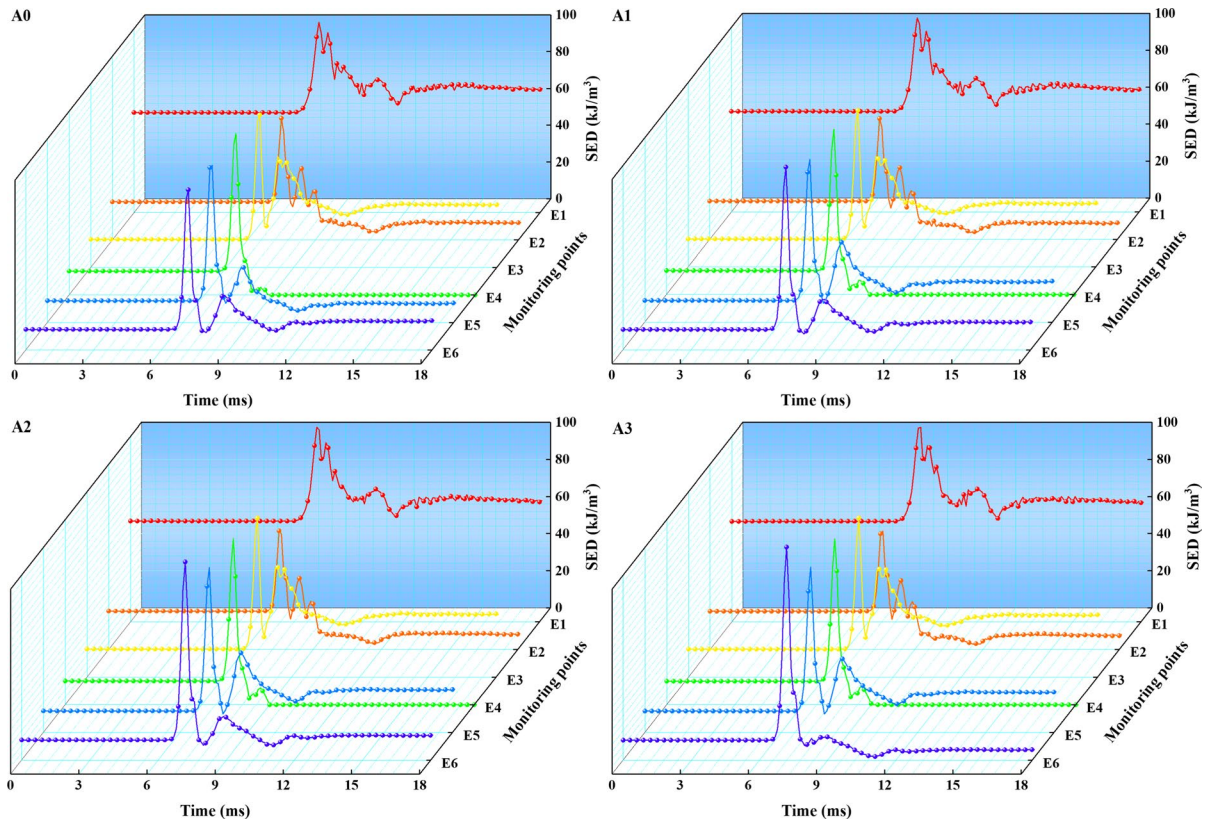

Fig. 9 SED evolution characteristics in explicit solution

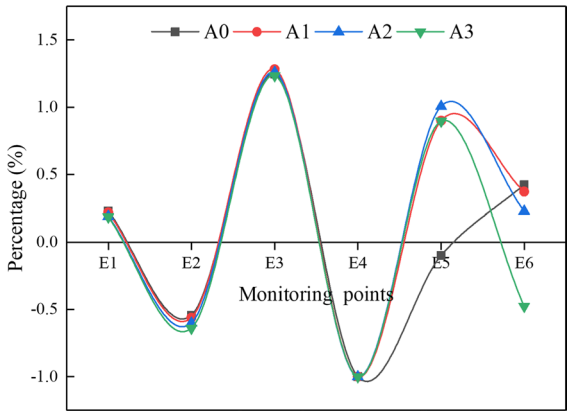

Fig. 10 Relative SED percentage change in group A

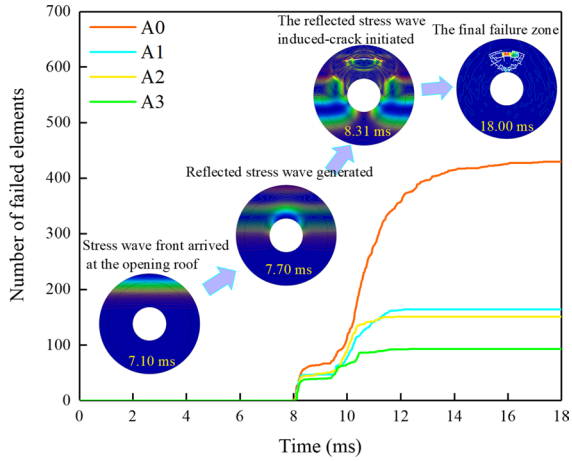

Fig. 11 Evolution of fracturing zone in the deep rock opening subjected to dynamic disturbance

3.2 Effect of microwave exposure time

3.2.1 SED evolution

Six monitoring points (E1, E2, E3, E4, E5, and E6, as shown in Fig. 7) were selected to monitor the SED evolution with distance from the roof. As Fig. 9 shows, the time-history of SED was constant before the arrival of the stress wave at the monitoring points, which demonstrated that the two-step simulation approach accurately transferred the static stress to the dynamic solution phase. In these four cases in group A, all the dynamic responses of the monitoring points were quite similar. Their responses can be divided into three phases in terms of SED evolution trend: (1) stationary phase before disturbance; (2) fluctuating phase during dynamic disturbance; (3) very slight fluctuation after disturbance, which mainly was caused by the reflected stress waves with low intensities. The duration of each phase varied with the location of the monitoring points. Because static stress does not exceed the rock strength, the dynamic response of elements started with an increase in the SED due to the elements absorbing the stress wave energy. After the dynamic disturbance, the change in SED depended upon the location. For example, in simulation A0, SED of E1, E3, and E6 stored more strain energy, and the change in SED at these points were 124.16 kJ/m^3, 18.97 kJ/m^3, and 4.75 kJ/m^3, respectively. The SED of E2, E4 and E5 decreased due to a release in strain energy, and the change in SED at these points was − 11.33 kJ/m^3, − 13.00 kJ/m^3 and − 1.19 kJ/m^3, respectively. Generally, strain energy stored in the rock after a dynamic disturbance may create a high proneness to rockbursts when subjected to further dynamic disturbances; rock-released strain energy may induce rock failure.

To eliminate the influence of the initial SED, the relative change percentage in SED was used to evaluate the change of SED for different cases, which is expressed as,

$$\text{Relative SED percentage change} = \frac{\text{Final SED} - \text{Initial SED}}{\text{Initial SED}} \times 100\% \tag{11}$$

As Fig. 10 shows, the strain energy of E4 was dissipated entirely in each of the four simulation cases, which indicated that rock in the vicinity of E4 (2.25 m from the roof) failed. The location of the maximum increment of SED was always E3 (1.58 m from the roof) for the four cases. The duration of the microwave exposure time affected the change in SED differently for the four cases. The strain energy was released at point E5 in case A0 but stored in A1, A2, and A3. The change in SED also demonstrated that the rock failure distribution around the opening is generally discontinuous (Qian and Zhou 2011).

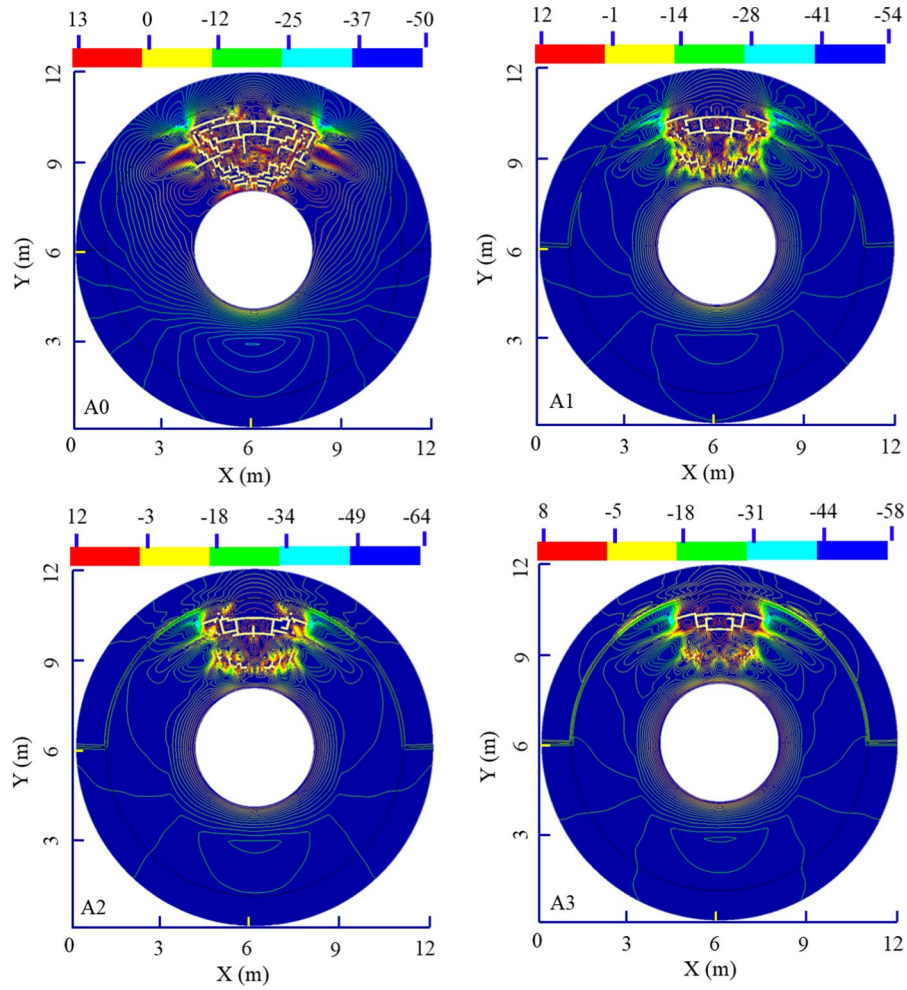

Fig. 12 Final fracturing zone around the circular opening subjected to dynamic disturbance (Group A)

3.2.2 Fracturing zone evolution

In the dynamic response simulation, the variation of the failed rock element numbers was tracked to observe the evolution of the fracturing zone induced by a stress wave. Cloud diagrams in Fig. 11 present the fracturing zone evolution of simulation case A0. For the untreated rock mass, a dramatic rockburst occurred in zone B. The incident stress wave arrived at the roof at 6.90 ms, and the element erosion initiated at 8.08 ms, indicating that the reflected tensile stress wave mainly drove the rockburst. Although rock properties govern the stress wave velocity, the rock element erosion of four simulation cases almost always initiated ~ 8 ms due to the finite size of MPZ. It was also observed that simulation case A0 had the most prolonged rock fracturing duration, with rock fracturing ending at 17.45 ms. In cases A1, A2, and A3, rock fracturing ended at 12.08 ms, 11.92 ms, and 12.69 ms, respectively.

Figure 12 shows the final failure patterns around the circular opening under different durations of microwave exposure treatment, where the contour lines denote the value of the major principal stress in MPa. The fracturing zone's shape was approximate to an inverted trapezoidal, and the rock fracturing zones in cases A1, A2, and A3 and were smaller than that in untreated case A0. Furthermore, the bottom boundary of the fracturing zone in cases A1, A2, and A3 deviated from the roof. Thus, the rock mass in the vicinity of the top free face could prevent the rock debris in the fracturing zone from falling into workspace directly. In addition, the rock fracturing caused a redistribution of the stress field around the fracturing zone, where tensile stress was observed in each simulation case. Furthermore, the maximum tensile

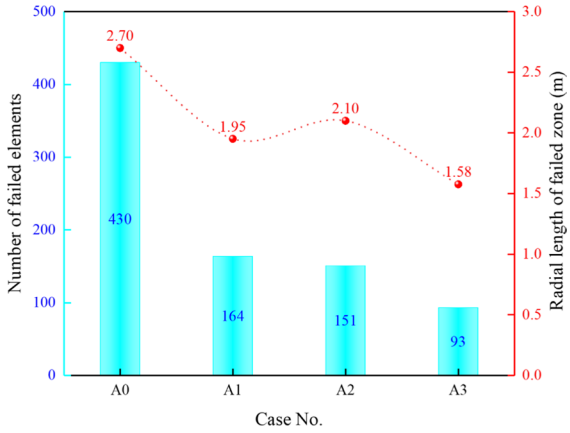

Fig. 13 Number of failed elements and radial length of the fracturing zone (Group A)

stress declined with increasing microwave exposure duration.

The number of failure elements in the fracturing zone has a negative relation with microwave exposure duration. When microwave exposure duration increased from 0 to 30 s, the number of failed elements decreased from 430 to 93. Zone B was meshed as a concentric circle, and thus, the radial length of the failed zone (the distance from top to bottom of the inverted trapezoidal) was used to measure the range of fracturing in different cases (Fig. 13). When zone A was treated with 30 s microwave exposure time, the radial length of the failed zone was approximately half of that in untreated case A0. Therefore, the feasibility of microwave destressing in a deep opening was numerically validated. Furthermore, a longer microwave treatment time can better prevent the occurrence of a rockburst event.

In Sect. 3.2, the effect of microwave exposure time on microwave destressing has been carefully discussed. Case A3 shows the weakest rockburst in group A. In subsequent sections, different layouts of MPZ on rockburst occurrence are discussed. Overall, the rock mechanical parameters for MPZ are consistent with case A3.

3.3 Effect of discontinuous layouts of MPZs

It is of critical to determine the range of MPZ, as the extent of MPZ affects the cost of microwave preconditioning to a zone. Therefore, reasonable layouts should be determined for implementation. Numerical simulation Group B was performed to determine the effect of a discontinuous distribution of MPZs on rockburst prevention. As Fig. 14 shows, the model setup was as follows: the area corresponding to zone A shown in Fig. 2 was divided into five, seven, and nine, evenly. Case No. was the name according to the number MPZs, i.e., B52 denotes the semi-annular zone was divided into five segments evenly, and two of which were MPZ and three were untreated rock masses.

As Fig. 15 shows, both monitoring locations E2 and E4 were where SED decreased in the six simulation cases. Moreover, the number of monitoring points where SED decreased after dynamic disturbing in cases B52, B74, and B94 were three (E2, E4, and E5), four (E2, E4, E5, and E6), and three (E2, E4, and E5), respectively. Overall, there were more locations with decreases in SED compared to B53, B73, and B95. According to the fracturing patterns shown in Fig. 14 and the radial length of the failed zone in Fig. 16, the range of the failed zone in simulation cases B52, B74, and B94 were more extensive than B53, B73, and B95. Comparing the layout of MPZ in those six cases, there was an MPZ directly above the opening roof in B53, B73, and B95. The different layouts of MPZ induced different redistributions of the geo-stress. Thus, each case has a different prerequisite for rockburst occurrence. In simulation cases B52, B74, and B94, no destressing zone was generated directly above zone B due to the interval between the top two MPZs. However, stress wave propagation efficiency has a vital effect on the stability of zone B. In B52, B74, and B94, the stress wave propagated to zone B directly through the surrounding untreated rock directly above zone B. Furthermore, in B53, B73, and B95, stress wave reflection occurred at the boundary of top MPZ and the surrounding rock, which led to the incident stress wave carrying less energy to zone B. Therefore, dynamic disturbance induced more dramatic dynamic failures in B52, B74, and B94 than cases B53, B73, and B95.

In practice, the blasting source location is known. Thus, considering the spatial location of protection required, the MPZ is suggested to be arranged on the connection line between the blasting source and the protection zone. As Fig. 16 shows, we can see that case B73 shows an optimal effect of rockburst prevention, as it had the least number of failed elements (63) and shortest radial length of the failed zone (1.50 m).

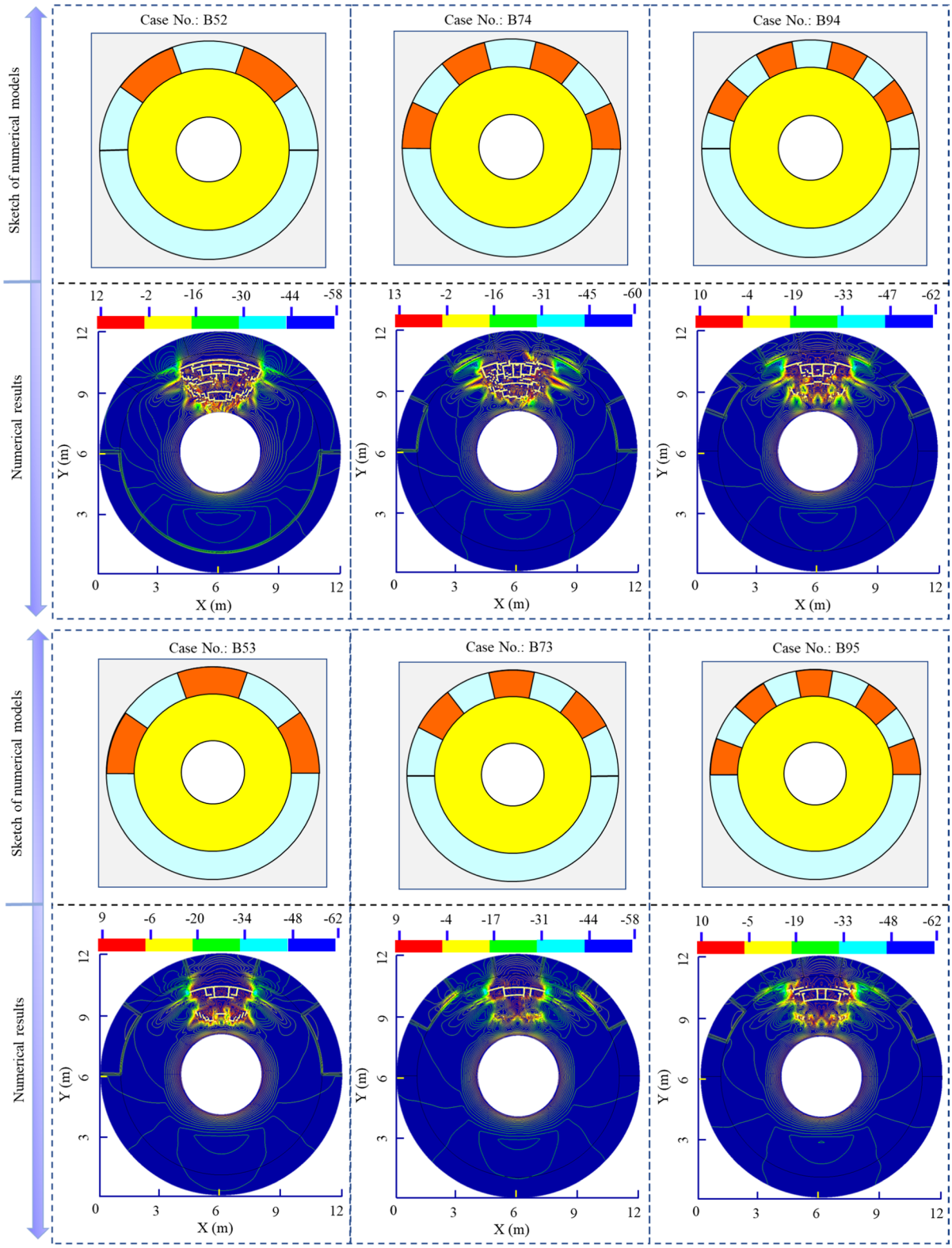

Fig. 14 Sketch of numerical model and fracturing zone around the circular opening (group B)

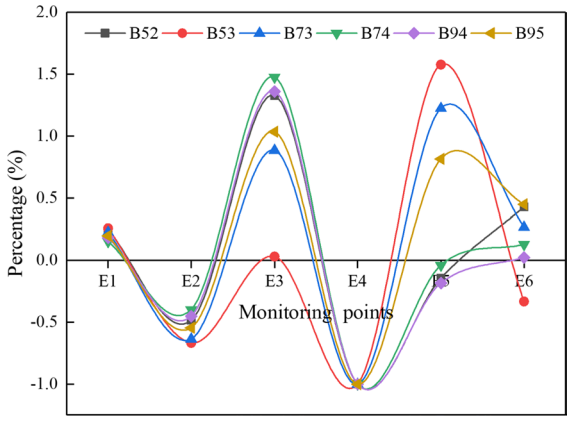

Fig. 15 Relative SED percentage change of group B

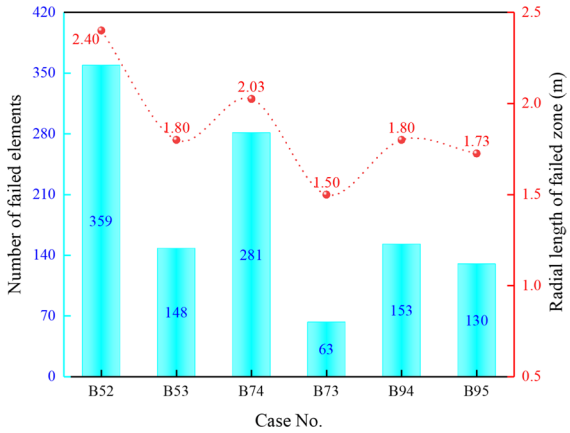

Fig. 16 Number of failed elements and radial length of the fracturing zone (Group B)

3.4 Effect of MPZ length

After the most effective position for applying MPZ for rockburst control was determined, group C was created to investigate the effect of MPZ length on rockburst intensity. The schematic diagram of the numerical model is shown in Fig. 17. A continuous MPZ was arranged above the zone B. α was increased from 20° to 160° at an interval of 20° to control the length of MPZ (the cases of α = 0° and 180° correspond to A0 and A3, respectively).

Similar to the results in groups A and B, SED at E2 and E4 decreased, and SED at E1 and E3 increased in each simulation case after the dynamic

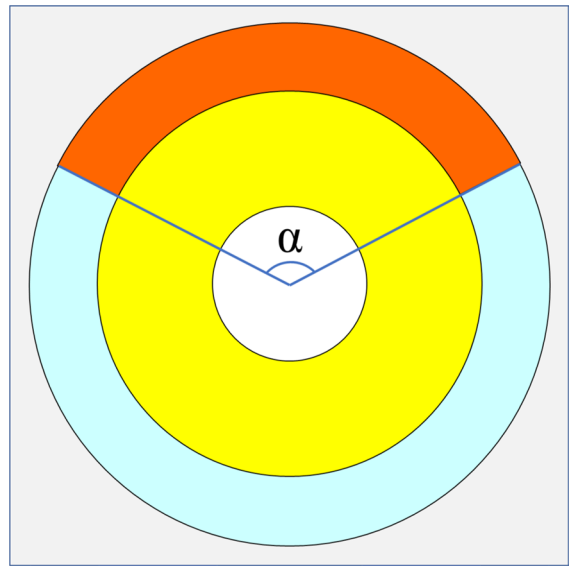

Fig. 17 Numerical model sketch of group C

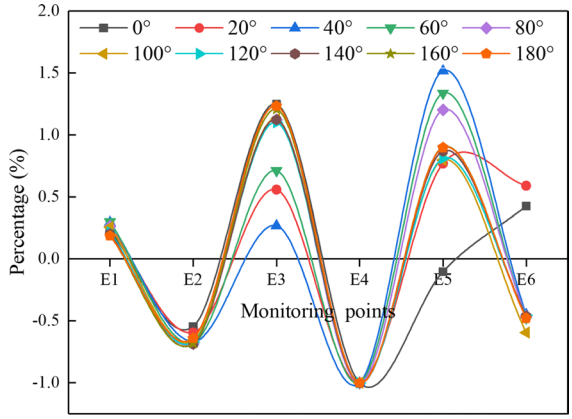

Fig. 18 Relative SED percentage change in group C

disturbance (Fig. 18). Furthermore, the strain energy at monitoring point E4 was completed released. Thus, the dynamic response between E1 and E4 in those simulation cases was mainly dominated by the initial static stress.

With the increasing MPZ length, more energy is reflected at the top boundary of MPZ, and consequently, less energy is exerted on zone B during the downward stress wave propagation. However, it is worth noting that the variations in the length of

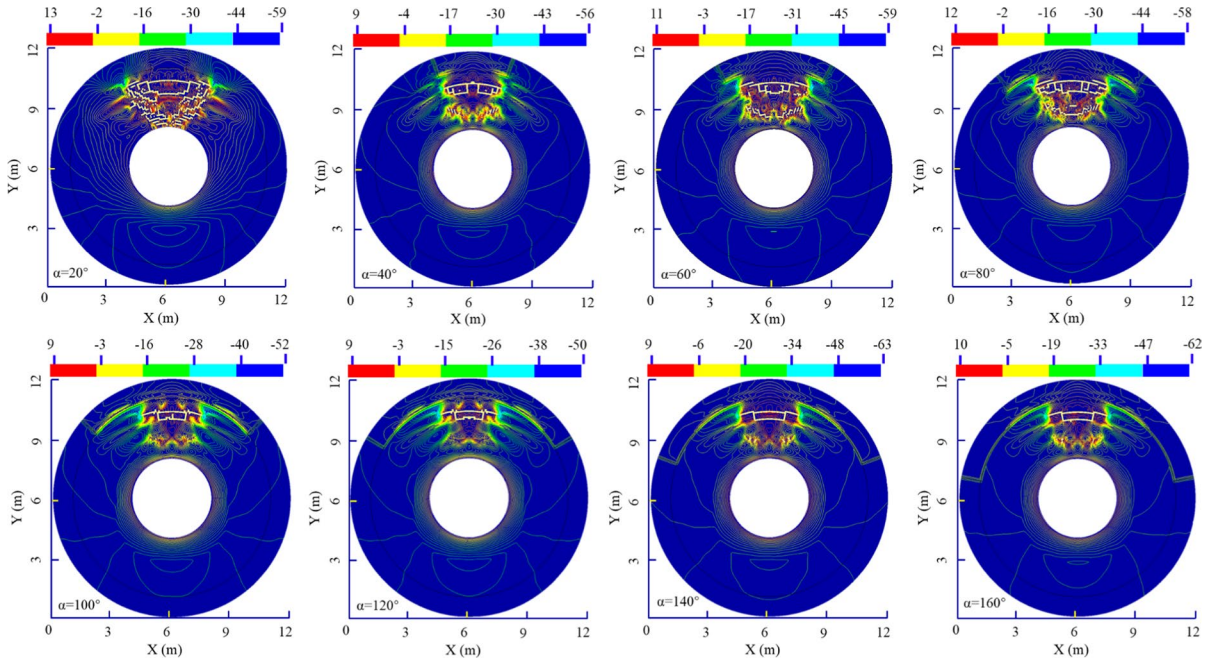

Fig. 19 Final fracturing zone around the circular opening subjected to dynamic disturbance in group C

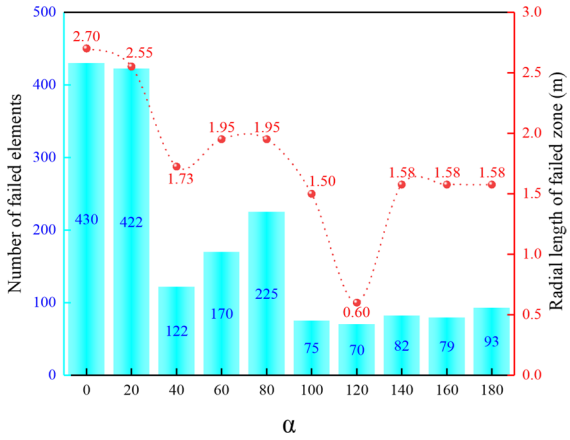

Fig. 20 Number of failed elements and radial length of the final fracturing zone (Group C)

MPZ also appear to govern the geo-stress distribution of the destressed zone. Therefore, the dynamic failure intensity has no constant negative relation with the MPZ length. As Fig. 19 shows, a dramatic rockburst occurred when α was 20°, and the fracturing zone extended to the roof. When α increased to 40°, the number of failed elements and the radial length of the failed zone decreased to 122 and 1.73 m, respectively (Fig. 20). The dynamic failure intensity increased when α varied from 40° to 80°. When α was 100°,140°, 160°, and 180°, the failure pattern and range of the fracturing zone were all quite similar, and the dynamic failure intensity was at a relatively low level. The lowest dynamic failure intensity occurred when α = 120°, which had the least number of failed elements (70) and shortest radial length of the fracturing zone (0.60 m). In practice, an overlong MPZ length leads to increased cost of the project and is a waste of energy; an optimal length to balance the cost of effectiveness needs to be found for each project.

Table 2 Numerical model dimensions of group D

Case No.	L_2 (m)	L_3 (m)
D1	2.50	1.00
D2	2.50	0.50
D3	3.50	1.00

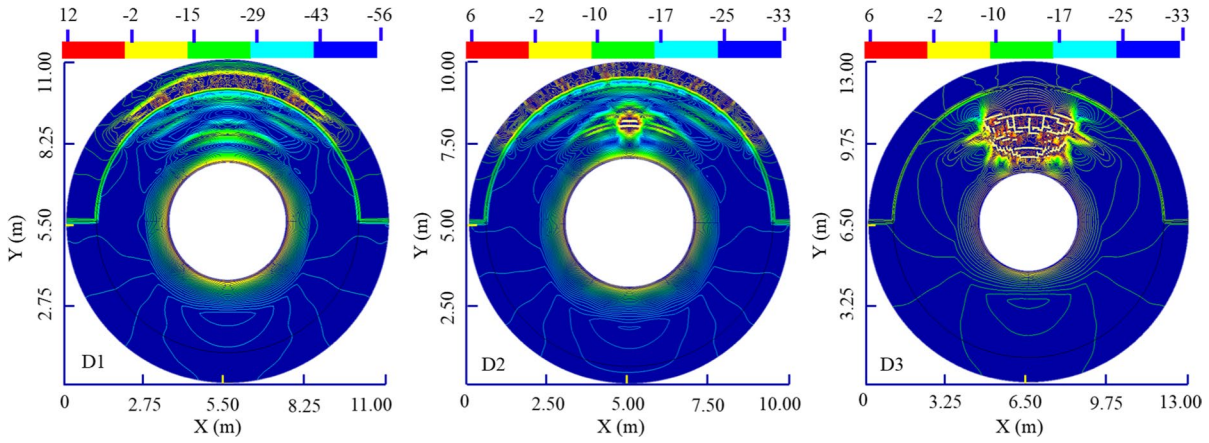

Fig. 21 Final fracturing zone around the circular opening subjected to dynamic disturbance in group D

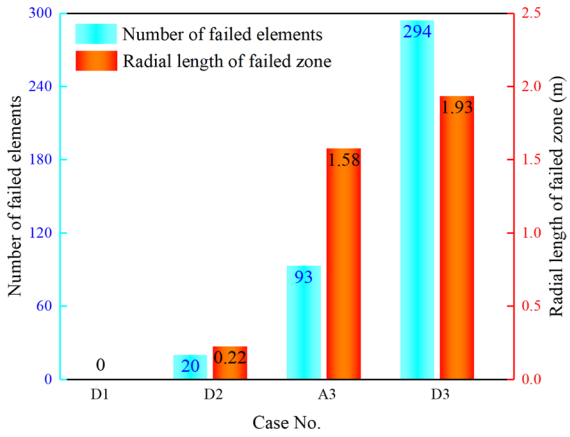

Fig. 22 Number of failed elements and the radial length of the final fracturing zone (Group D)

3.5 Effect of MPZ width and its distance from the roof

Numerical simulation group D consisted of altering L_2 and L_3 to study the effect of MPZ width and its position on the dynamic fracturing behavior around the opening. The model dimensions are as listed in Table 2.

Compared with the model dimension of simulation case A3, the distance between MPZ and the opening roof was changed to 2.50 m (D1) and 3.50 m (D3), respectively. It was observed that the dynamic failure intensity in simulation case D3 was much more intense than A3 (Figs. 21 and 22). The increase in L_2 caused the destressed zone governed by MPZ to move away from the free surface. Accordingly, the stress redistribution surrounding the opening became more evident. It can be deduced that further from the roof, MPZ may not work for dynamic failure control, and the fracturing pattern should closely mimic simulation case A0. When L_2 decreased to 2.50 m, no dynamic failure around the opening was generated, indicating that the destressing zone caused by MPZ overlapped with the initial high static stress zone. Therefore, the coupling of the static and dynamic stresses did not reach the rock strength. Based upon case D1, the effect of MPZ width was examined by reducing L_3 by an interval of 0.10 m. When L_3 was reduced to 0.5 m, the rock mass did not fail. After that, the amplitude of the dynamic disturbance increased from 120 to 130 MPa in case D2, where slight dynamic failure occurred. 20 elements failed, and the radial length of the failed zone was 0.22 m for case D2.

Overall, when the MPZ is closer to the free face, there is a less dynamic hazardous risk around the opening. However, the fracturing zone induced by microwave treatment also plays a vital role in the static stability of zone B. Too short of a distance of MPZ from the roof may result in zone B unable to support the overburden rock mass.

4 Discussion

This paper introduced a novel rock prevention technology by microwave destressing, and verified its

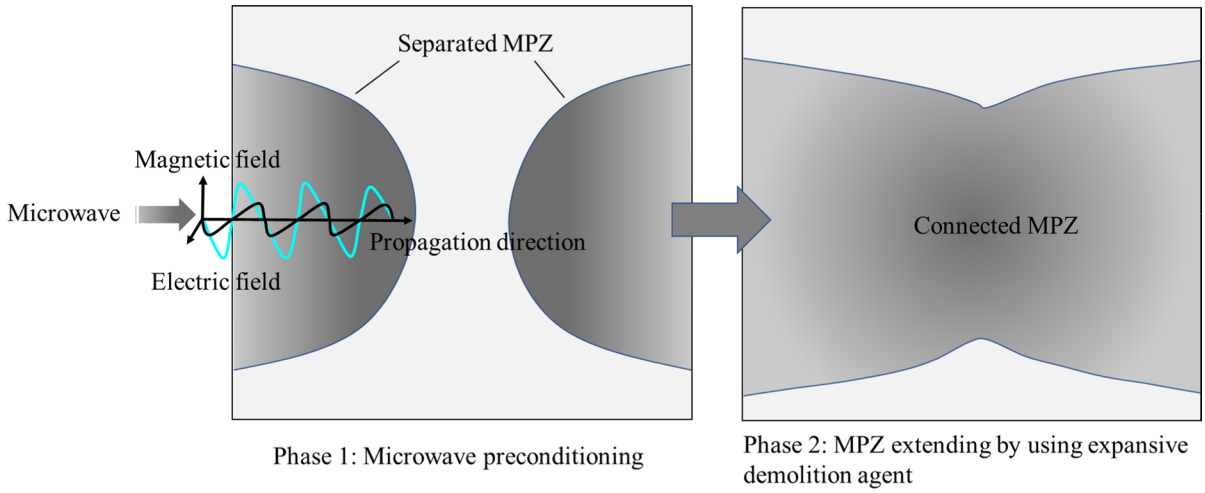

Fig. 23 Sketch of the construction of a continuous MPZ by quasi-static rock breakage technology

applicability numerically. However, the limitations of this study should be pointed out to guide future successful field experiments and practices. Numerical simulations were performed using the FEM model based on the assumption that rock is a continuous medium (Liu et al. 2019). Experimental results indicated that microwave-induced cracks are randomly distributed throughout the rock mass (Wei et al. 2019). As reported by Lu et al., the sample surface exhibits fewer cracks during shorter exposure times (at 5 kW and 10 s). As the radiation time increases (20 s and 30 s), cracks gradually propagate, and their number grows. The primary crack on the curved surface runs roughly parallel to the long axis of the cylinder, extending towards the end face and connecting with the crack observed on the end face (Lu et al. 2020). It is known that discontinuities in geotechnical engineering can negatively impact the efficiency of stress wave propagation (Shen et al. 2021). Therefore, the numerical results of microwave destressing in this study are relatively conservative. For instance, microwave treatments could potentially cause less rock dynamic failure or even no failure if the same structural parameters of the MPZ for simulation case A3 are in place. Although a discontinuous arrangement of the MPZ is advantageable due to its low economic cost and energy saving, a continuous MPZ may be more suitable for engineering practice that faces multiple dynamic disturbances from different orientations, such as a deep mine with multistope production models. Because microwave energy exponentially decays within a material, the range of weakening of the rock mass due to microwave treatments is limited in its physical depth into the material (Hassani et al. 2016). The microwave penetration depth D_p is defined as the distance at which microwave power is reduced to 1/e (e = 2.718) from the strength at the point of entry, and can be calculated as (Tang 2015),

$$D_p = \frac{\lambda_0}{2\pi\sqrt{2\varepsilon'\left[\sqrt{1+\left(\frac{\varepsilon''}{\varepsilon'}\right)^2}-1\right]}} \tag{12}$$

where λ_0 is the wavelength in free space, ε' and ε'' are dielectric constant and loss factor, respectively, of rock materials. According to Eq. (12), the microwave penetration depth in rock materials and microwave wavelength is of the same magnitude. For a given rock material, the microwave penetration depth ranges from a few centimeters to a few tens of centimeters under the action of two industrial microwave frequencies (915 and 2450 MHz). For the cases with L_3 of 1 m in practice, multipoint microwave destressing operations in the radius and circumferential direction of MPZs are needed, which could negatively affect the cost and efficiency. As a consequence, to address this, an improved scenario is proposed as Fig. 23.

First, high-powered microwaves are used to construct a discontinuous MPZ. A non-explosive,

expansive demolition agent is then injected into the bottom of the destressing boreholes to expand the dimensions of the cracks induced by microwave treatment, causing the separated MPZs to connect into a continuous MPZ (Zhang et al. 2021c, 2020). It is worth noting that the microwave-induced cracks dominate the expansion direction of the MPZ under the action of the expansive demolition agent. Thus, to cause the expanded cracks to propagate towards the adjacent MPZ, both sides of the MPZ should be treated with longer microwave irradiation times to increase the number of cracks generated. Analogously, technologies such as hydraulic fracturing and supercritical CO_2 fracturing can be considered as potential measures for connecting MPZs in large-scale rock engineering (Chen et al. 2021; Zhang et al. 2021a). As a quasi-static destressing technique, microwave destressing introduces fewer dynamic disturbances to the surrounding rock, which opens up numerous aspects worthy of research.

5 Conclusions

The feasibility of microwave destressing in deep circular openings is numerically validated based on an impact-induced rockburst FEM model. Due to the rock mass being simplified as a continuum medium, the numerical results of microwave destressing in this study are conservative. The two main functions of MPZ on rockburst prevention can be summarized as follows: a destressed zone below the MPZ reduces the stress level around the opening, where rock needs more energy to achieve its strain energy storage limit when subjected to dynamic disturbance; the MPZ deformation and stress wave reflection at the boundary of the MPZ and the surrounding rock lead to the reduction of stress transmission efficiency. Thus, the stress waves carry less energy that can be exerted on the rock around the opening.

Both the spatial layout and geometrical parameters of MPZ significantly affect the microwave destressing effect. Overall, the main conclusions are as follows:

(1) Group A: Within 4 m to the roof, microwave treatment induced a decrease in the stress level. In Case A3, there are a minimum of 93 failed elements, and the shortest radial length of the fracturing zone is 1.58 m among group A. The introduction of the MPZ improved the safety conditions surrounding the opening. A longer microwave irradiation time in the MPZ results in a smaller failure intensity induced by the dynamic disturbance around the deep opening.
(2) Group B: In cases B52, B74, and B94, the stress wave propagated directly to zone B through the surrounding untreated rock above zone B, resulting in a relatively higher dynamic failure intensity in Group B. The optimal MPZ should be strategically arranged along the connection line between the protective target and the blasting source, as demonstrated in cases B53, B73, and B95. These configurations showcase the effectiveness of discontinuous MPZs, offering both energy and cost savings in practice, making them suitable for applications with known and fixed blasting sources.
(3) Group C: As α varies from 0° to 180°, the lowest dynamic failure intensity occurred when $\alpha = 120°$, exhibiting the least number of failed elements (70) and the shortest radial length of the fracturing zone (0.60 m). However, due to the rockburst occurrence governed by the coupling effect of geo-stress and dynamic disturbance, the dynamic failure intensity around the opening does not always exhibit a negative relationship with the MPZ length. In scenarios with multiple blasting sources and variable positions, a continuous MPZ is deemed appropriate for optimal performance.
(4) Group D: When L_2 decreased from 3.5 m to 2.50 m, no dynamic failure around the opening was observed in case D1, suggesting that a closer distance of the MPZ from the free face results in a more effective microwave destressing effect. However, the closer proximity of the MPZ to the free face also introduces more adverse effects on the static stability of zone B. A distance that is too short may lead to zone B being unable to support the overburden rock mass.

Acknowledgements This study was funded by the National Natural Science Foundation of China (Project no. 52204167), Open Research Fund of State Key Laboratory of Safety Technology of Metal Mines (Project no. kfkt2023-04), the Natural Science Foundation of Jiangsu Province (Project no. BK20231071), the Jiangsu Provincial Association for Science and Technology Youth Science and Technology Talent

Support Project (Project no. JSTJ-2023-XH036), the Fundamental Research Funds for the Central Universities (Project no. 2023QN1001), and State key Laboratory of Mining Disaster Prevention and Control (Shandong University of Science and Technology), Ministry of Education (Project no. JMDPC202402). The first author also expresses his gratitude for the financial support received from the China Scholarship Council and the high-performance computer support received from Compute Canada. The contribution of the Geomechanics Lab of McGill University is acknowledged.

Declarations

Competing interests The authors declare that they have no conflicts of interest.

References

Cai M (2019) Rock support in strainburst-prone ground. Int J Min Sci Technol 29(4):529–534. https://doi.org/10.1016/j.ijmst.2019.06.008

Chen T, Zheng X, Qiu X, Feng X-T, Elsworth D, Cui G, Jia Z, Pan Z (2021) Experimental study on the feasibility of microwave heating fracturing for enhanced shale gas recovery. J Nat Gas Sci Eng 94:104073. https://doi.org/10.1016/j.jngse.2021.104073

Drover C, Villaescusa E, Onederra I (2018) Face destressing blast design for hard rock tunnelling at great depth. Tunn Undergr Space Technol 80:257–268. https://doi.org/10.1016/j.tust.2018.06.021

Feng XT, Liu JP, Chen BR, Xiao YX, Feng GL, Zhang FP (2017) Monitoring, warning, and control of rockburst in deep metal mines. Engineering 3(4):538–545. https://doi.org/10.1016/J.ENG.2017.04.013

Feng XT, Zhang JY, Yang CX, Tian J, Lin F, Li SP, Su XX (2021) A novel true triaxial test system for microwave-induced fracturing of hard rocks. J Rock Mech Geotech Eng. https://doi.org/10.1016/j.jrmge.2021.03.008

Gong QM, Yin LJ, Wu SY, Zhao J, Ting Y (2012) Rock burst and slabbing failure and its influence on TBM excavation at headrace tunnels in Jinping II hydropower station. Eng Geol 124:98–108. https://doi.org/10.1016/j.enggeo.2011.10.007

Guo W, Fan W, Shao XD, Shen DJ, Chen BS (2018) Constitutive model of ultra-high-performance fiber-reinforced concrete for low-velocity impact simulations. Compos Struct 185:307–326. https://doi.org/10.1016/j.compstruct.2017.11.022

Guo DP, Chen HM, Tang LB, Chen ZX, Samui P (2021) Assessment of rockburst risk using multivariate adaptive regression splines and deep forest model. Acta Geotech. https://doi.org/10.1007/s11440-021-01299-2

Hassani F, Nekoovaght PM, Gharib N (2016) The influence of microwave irradiation on rocks for microwave-assisted underground excavation. J Rock Mech Geotech Eng 8(1):1–15. https://doi.org/10.1016/j.jrmge.2015.10.004

He MC, Xia HM, Jia XN, Gong WL, Zhao F, Liang KY (2012) Studies on classification, criteria and control of rockbursts. J Rock Mech Geotech Eng 4(2):97–114. https://doi.org/10.3724/SP.J.1235.2012.00097

He MC, Ren FQ, Liu DQ (2018) Rockburst mechanism research and its control. Int J Min Sci Technol 28(5):829–837. https://doi.org/10.1016/j.ijmst.2018.09.002

Hu XD, Zhao GF, Deng XF, Hao YF, Fan LF, Ma GW, Zhao J (2018) Application of the four-dimensional lattice spring model for blasting wave propagation around the underground rock cavern. Tunn Undergr Space Technol 82:135–147. https://doi.org/10.1016/j.tust.2018.08.006

Hu GZ, Wang CB, Xu JL, Wu XF, Qin W (2021) Experimental investigation on decreasing burst tendency of hard coal using microwave irradiation. J China Coal Soc 46(02):450–465. https://doi.org/10.13225/j.cnki.jccs.XR20.1906

Jones DA, Kingman SW, Whittles DN, Lowndes IS (2005) Understanding microwave assisted breakage. Miner Eng 18(7):659–669. https://doi.org/10.1016/j.mineng.2004.10.011

Ju Y, Zhu Y, Zhou H, Ge S, Xie H (2021) Microwave pyrolysis and its applications to the in situ recovery and conversion of oil from tar-rich coal: an overview on fundamentals, methods, and challenges. Energy Rep 7:523–536. https://doi.org/10.1016/j.egyr.2021.01.021

Kahraman S, Canpolat AN, Fener M (2020) The influence of microwave treatment on the compressive and tensile strength of igneous rocks. Int J Rock Mech Min Sci 129:104303. https://doi.org/10.1016/j.ijrmms.2020.104303

Khan M, He X, Farid A, Song D, Li Z, Tian X, Ni M (2021) A novel geophysical method for fractures mapping and risk zones identification in a coalmine, Northeast, China. Energy Rep 7:3785–3804. https://doi.org/10.1016/j.egyr.2021.06.071

Konicek P, Saharan MR, Mitri H (2011) Destress blasting in coal mining—State-of-the-art review. Procedia Engineering 26:179–194. https://doi.org/10.1016/j.proeng.2011.11.2157

Li CJ, Li XB (2018) Influence of wavelength-to-tunnel-diameter ratio on dynamic response of underground tunnels subjected to blasting loads. Int J Rock Mech Min Sci 112:323–338. https://doi.org/10.1016/j.ijrmms.2018.10.029

Li X, Li XF, Zhang QB, Zhao J (2018) A numerical study of spalling and related rockburst under dynamic disturbance using a particle-based numerical manifold method (PNMM). Tunn Undergr Space Technol 81:438–449. https://doi.org/10.1016/j.tust.2018.08.026

Li CJ, Li XB, Liang LS (2020a) Dynamic response of existing tunnel under cylindrical unloading wave. Int J Rock Mech Min Sci 131:104342. https://doi.org/10.1016/j.ijrmms.2020.104342

Li X, Wang S, Xu Y, Yao W, Xia KW, Lu GM (2020b) Effect of microwave irradiation on dynamic mode-I fracture parameters of Barre granite. Eng Fract Mech 224:106748. https://doi.org/10.1016/j.engfracmech.2019.106748

Liu KW, Li XD, Hao H, Li XB, Sha YY, Wang WH, Liu XL (2019) Study on the raising technique using one blast based on the combination of long-hole presplitting and vertical crater retreat multiple-deck shots. Int J Rock Mech Min Sci 113:41–58. https://doi.org/10.1016/j.ijrmms.2018.11.012

Lu GM, Li YH, Hassani F, Zhang X (2017) The influence of microwave irradiation on thermal properties of main rock-forming minerals. Appl Therm Eng 112:1523–1532. https://doi.org/10.1016/j.applthermaleng.2016.11.015

Lu GM, Feng XT, Li YH, Zhang XW (2019a) The microwave-induced fracturing of hard rock. Rock Mech Rock Eng 52(9):3017–3032. https://doi.org/10.1007/s00603-019-01790-z

Lu GM, Feng XT, Li YH, Hassani F, Zhang XW (2019b) Experimental investigation on the effects of microwave treatment on basalt heating, mechanical strength, and fragmentation. Rock Mech Rock Eng 52(8):2535–2549. https://doi.org/10.1007/s00603-019-1743-y

Lu G, Feng X, Li Y, Zhang X (2020) Influence of microwave treatment on mechanical behaviour of compact basalts under different confining pressures. J Rock Mech Geotech Eng 12(2):213–222

Luo Y, Xu K, Huang JH, Li XP, Liu TT, Qu DX, Chen PP (2021) Impact analysis of pressure-relief blasting on roadway stability in a deep mining area under high stress. Tunn Undergr Space Technol 110:103781. https://doi.org/10.1016/j.tust.2020.103781

Manouchehrian A, Cai M (2018) Numerical modeling of rockburst near fault zones in deep tunnels. Tunn Undergr Space Technol 80:164–180. https://doi.org/10.1016/j.tust.2018.06.015

Mazaira A, Konicek P (2015) Intense rockburst impacts in deep underground construction and their prevention. Can Geotech J 52(10):1426–1439. https://doi.org/10.1139/cgj-2014-0359

Meisels R, Toifl M, Hartlieb P, Kuchar F, Antretter T (2015) Microwave propagation and absorption and its thermo-mechanical consequences in heterogeneous rocks. Int J Miner Process 135:40–51. https://doi.org/10.1016/j.minpro.2015.01.003

Pan YS, Wang J, Zhang JZ, Song YM, Xiao YH, Wang HY (2022) Development and application of a hydraulic impact test machine for simulating rockburst conditions. Geomech Geophys Geo-Energy Geo-Resour 8(3):105. https://doi.org/10.1007/s40948-022-00363-9

Perras MA, Diederichs MS (2014) A review of the tensile strength of rock: concepts and testing. Geotech Geol Eng 32(2):525–546

Qian Q, Zhou X (2011) Quantitative analysis of rockburst for surrounding rocks and zonal disintegration mechanism in deep tunnels. J Rock Mech Geotech Eng 3(1):1–9. https://doi.org/10.3724/SP.J.1235.2011.00001

Sainoki A, Emad MZ, Mitri HS (2017) Study on the efficiency of destress blasting in deep mine drift development. Can Geotech J 54(4):518–528. https://doi.org/10.1139/cgj-2016-0260

Shen WL, Shi GC, Wang YG, Bai JB, Zhang RF, Wang XY (2021) Tomography of the dynamic stress coefficient for stress wave prediction in sedimentary rock layer under the mining additional stress. Int J Min Sci Technol. https://doi.org/10.1016/j.ijmst.2021.04.003

Sheorey P (1994) A theory for in situ stresses in isotropic and transverseley isotropic rock. Int J Rock Mech Min Sci 31(1):23–34. https://doi.org/10.1016/0148-9062(94)92312-4

Tang JM (2015) Unlocking potentials of microwaves for food safety and quality. J Food Sci 80(8):E1776–E1793. https://doi.org/10.1111/1750-3841.12959

Tang ZL, Yao W, Zhang JC, Xu QJ, Xia KW (2019) Experimental evaluation of PMMA simulated tunnel stability under dynamic disturbance using digital image correlation. Tunn Undergr Space Technol 92:103039. https://doi.org/10.1016/j.tust.2019.103039

Tang MY, Gao MZ, Li SW, Yang BG, Tang RF, Li F, Liu JJ (2023a) Failure behavior and energy evolution characteristics of deep roadway sandstone under different microwave irradiation modes. J Central South Univ 30(1):214–226. https://doi.org/10.1007/s11771-023-5237-4

Tang S, Li J, Tang L, Zhang L (2023b) Microseismic monitoring and experimental study on rockburst in water-rich area of tunnel. Tunn Undergr Space Technol 141:105366. https://doi.org/10.1016/j.tust.2023.105366

Vazaios I, Diederichs MS, Vlachopoulos N (2019) Assessment of strain bursting in deep tunnelling by using the finite-discrete element method. J Rock Mech Geotech Eng 11(1):12–37. https://doi.org/10.1016/j.jrmge.2018.06.007

Vennes I, Mitri H, Chinnasane DR, Yao M (2021) Effect of stress anisotropy on the efficiency of large-scale destress blasting. Rock Mech Rock Eng 54(1):31–46. https://doi.org/10.1007/s00603-020-02252-7

Wang S, Xu Y, Xia KW, Tong TY (2021) Dynamic fragmentation of microwave irradiated rock. J Rock Mech Geotech Eng 13(2):300–310. https://doi.org/10.1016/j.jrmge.2020.09.003

Wang CB, Si GY, Zhang CG, Cao A, Canbulat I (2022) Ground motion characteristics and their cumulative impacts to burst risks in underground coal mines. Geomech Geophys Geo-Energy Geo-Resour 8(1):39. https://doi.org/10.1007/s40948-022-00340-2

Wei W, Shao ZS, Zhang YY, Qiao RJ, Gao JP (2019) Fundamentals and applications of microwave energy in rock and concrete processing—a review. Appl Therm Eng 157:113751. https://doi.org/10.1016/j.applthermaleng.2019.113751

Xu P, Shao J, Fan D, Chang J, Zhang N (2022) Analysis of pressure relief effect of borehole in rock burst mine. Energy Rep 8:156–161. https://doi.org/10.1016/j.egyr.2021.11.035

Yang C, Zhou KP, Gao RG, Xiong X (2021) Numerical investigation of the dynamic response of a preconditioned roof in an underground mine: a case study of mining environment regeneration. Soil Dyn Earthq Eng 140:106457. https://doi.org/10.1016/j.soildyn.2020.106457

Yang C, Hassani F, Zhou K, Gao F, Topa A (2022a) SPH-FEM simulations of microwave-treated basalt strength. Trans Nonferrous Metals Soc China 32(6):2003–2018. https://doi.org/10.1016/S1003-6326(22)65926-0

Yang C, Hassani F, Zhou KP, Xiong X, Wang FM, Shao Y (2022b) Effect of microwave treatment on the thermal properties and dynamic splitting behavior of red sandstone. Can Geotech J 59(7):1231–1242. https://doi.org/10.1139/cgj-2021-0313

Yang C, Hassani F, Zhou K, Zhang Q, Wang F, Gao F, Topa A (2022c) Numerical investigation of TBM disc cutter cutting on microwave-treated basalt with an unrelieved model. Arch Civil Mech Eng 22(3):147. https://doi.org/10.1007/s43452-022-00463-z

Zhang GH, Jiao YY, Wang H (2014) Outstanding issues in excavation of deep and long rock tunnels: a case study. Can Geotech J 51(9):984–994. https://doi.org/10.1139/cgj-2013-0087

Zhang Q, He MC, Wang J, Guo S, Guo ZB, Liu XY, Hu JZ, Ma ZM, Fan LX, Guo PF (2020) Instantaneous expansion with a single fracture: a new directional rock-breaking technology for roof cutting. Int J Rock Mech Min Sci 132:104399. https://doi.org/10.1016/j.ijrmms.2020.104399

Zhang CP, Liu S, Ma ZY, Ranjith PG (2021a) Combined micro-proppant and supercritical carbon dioxide (SC-CO2) fracturing in shale gas reservoirs: A review. Fuel 305:121431. https://doi.org/10.1016/j.fuel.2021.121431

Zhang LM, Cong Y, Meng FZ, Wang ZQ, Zhang P, Gao S (2021b) Energy evolution analysis and failure criteria for rock under different stress paths. Acta Geotech 16(2):569–580. https://doi.org/10.1007/s11440-020-01028-1

Zhang Q, Wang J, Guo S, Gong WL, Feng LF, Wang HS, Ming C, Ma ZM (2021c) Shaped charge hydraulic blasting: an environmental, safe, and economical method of directional roof cutting. Geofluids 2021:5511081. https://doi.org/10.1155/2021/5511081

Zhang J, Feng XT, Yang C, Lin F, Li S, Tong T, Su X (2022) The characteristics and mechanism of microwave-induced borehole fracturing of hard rock under true triaxial stress. Eng Geol 306:106768. https://doi.org/10.1016/j.enggeo.2022.106768

Zhao QH, Zhao XB, Zheng YL, Li JC, He L, He JL, Zou CJ (2020) Heating characteristics of igneous rock-forming minerals under microwave irradiation. Int J Rock Mech Min Sci 135:104519. https://doi.org/10.1016/j.ijrmms.2020.104519

Zheng YL, Zhao XB, Zhao QH, Li JC, Zhang QB (2020) Dielectric properties of hard rock minerals and implications for microwave-assisted rock fracturing. Geomech Geophys Geo-Energy Geo-Resour 6(1):22. https://doi.org/10.1007/s40948-020-00147-z

Zhou XP, Xiao N (2018) Analyzing fracture properties of the 3D reconstructed model of porous rocks. Eng Fract Mech 189:175–193. https://doi.org/10.1016/j.engfracmech.2017.10.021

Zhou XP, Xiao N (2019) Analysis of fracture properties of three-dimensional reconstructed rock model using hierarchical-fractal annealing algorithm. Eng Geol 256:39–56. https://doi.org/10.1016/j.enggeo.2019.04.017